a small-signal modulation ($M = \pi V/V_\pi$) at ω, is given by

$$E(t) = \frac{E_0}{2}\exp\left(i(\omega_0 t) + \frac{\pi}{2}\right) + \frac{E_0}{2}\sum_{n=-\infty}^{\infty} J_n(M)\exp(i(\omega_0 + n\omega)t)$$

where E_0 is the amplitude of the electric field before the modulator, ω_0 is the carrier frequency, and J_n is the Bessel function of order n. The sum corresponds to all of the sidebands at $\pm n\omega$. When the modulated beam goes through the filter, each electric field component is attenuated differently, depending on its frequency relative to the optical transfer function. Assuming a symmetric situation where the carrier frequency corresponds to a maximum of the optical transfer function, the components of the intensity at ω and at 2ω detected in the photodetector are proportional to

$$I(\omega) = 4J_1(M)H(1)H(0)\sin(\omega t)$$

$$I(2\omega) = \left[-2J_1^2(M)H^2(1) + 4\sum_{n=0}^{\infty} J_n(M)H(n)J_{n+2}(M)H(n+2)\right]\cos(2\omega t)$$

where $H(n)$ represents the value of the transfer function at $\omega_0 \pm n\omega$. In the absence of the filter, all of the $H(n)$ are equal to 1, and the modulation at 2ω vanishes due to the fact that $[-2J_1^2(M) + 4\sum_{n=0}^{\infty} J_n(M)J_{n+2}(M)] = 0$. This is not the case when the filter is present, in which case a term at 2ω is present. The coherent filter generates second-order (and other even-order) harmonics. This is a general property of filters that operate on the optical carrier's electric field (rather than intensity), and limits the application of such devices to a suboctave system where the generation of higher harmonics is of no consequence.

In summary, we have demonstrated a new optically coherent photonic microwave filter. The device consists of three coupled ring resonators integrated using silica technology. The optical phase in each ring is controlled using a thermo-optic phase shifter. The filter response can be shaped by either changing the laser wavelength or by using an integrated thermo-optic phase shifter. A passband transfer function centered at 15 GHz, flat within 0.4 dB over 1 GHz, is demonstrated.

ACKNOWLEDGMENT

This work was supported in part by the Joint Services Electronics Program (JSEP) and by the Office of Naval Research (ONR/MURI).

REFERENCES

1. K.P. Jackson, S.A. Newton, B. Moslehi, M. Tur, C.C. Cutler, J.W. Goodman, and H.J. Shaw, Optical fiber delay-line signal processing, IEEE Trans Microwave Theory Tech MTT-33 (1985), 193–209.
2. M.Y. Frankel and R.D. Esman, Fiber-optic tunable microwave transversal filter, IEEE Photon Technol Lett 7 (1995), 191–193.
3. C.T. Chang, J.A. Cassaboom, and H.F. Taylor, Fibre-optic delay-line devices for R.F. signal processing, Electron Lett 13 (1977), 678–680.
4. F. Coppinger, S. Yegnanarayanan, P.D. Trinh, B. Jalali, and I.L. Newberg, Nonrecursive tunable photonic filter using wavelength-selective true time delay, IEEE Photon Technol Lett 8 (1996), 1214–1216.
5. B. Moslehi and J.W. Goodman, Novel amplified fiber-optic recirculating delay line processor, J Lightwave Technol 10 (1992), 1142–1147.
6. M.C. Vàzquez, B. Vizoso, M. Lòpez-Amo, and M.A. Muriel, Single and double amplified recirculating delay lines as fibre-optic filters, Electron Lett 28 (1992), 1017–1019.
7. D.B. Hunter and R.A. Minasian, Photonic signal processing of microwave signals using an active-fiber Bragg-grating-pair structure, IEEE Trans Microwave Theory Tech 45 (1997), 1463–1466.
8. S. Sales, J. Capmany, J. Marti, and D. Pastor, Experimental demonstration of fibre-optic delay line filters with negative coefficients, Electron Lett 31 (1995), 1095–1096.
9. F. Coppinger, S. Yegnanarayanan, P.D. Trinh, and B. Jalali, All-optical incoherent negative taps for photonic signal processing, Electron Lett 33 (1997), 973–975.
10. B.A. Ferguson and C.L. Chen, Optical fiber recirculating delay lines as controllable radio frequency notch filters, J Lightwave Technol 11 (1993), 1539–1544.
11. K. Sasayama, M. Okuno, and K. Habara, Coherent optical transversal filter using silica-based waveguides for high-speed signal processing, J. Lightwave Technol 9 (1991).
12. C.K. Madsen and J.H. Zhao, A general planar waveguide autoregressive optical filter, J Lightwave Technol 14 (1996), 437–447.
13. C.K. Madsen and J.H. Zhao, Planar waveguide AR lattice filters: Advantages and challenges, Integrated Photonics Res, 1996 Tech Dig Ser, Vol. 6, Proc Integrated Photonics, Boston, MA, Apr. 1996, pp. 167–170.
14. C.K. Madsen and J.H. Zhao, Postfabrication optimization of an autoregressive planar waveguide lattice filter, Appl Opt 36 (1997), 642–647.

SOURCE EXCITATION METHODS FOR THE FINITE-DIFFERENCE TIME-DOMAIN MODELING OF CIRCUITS AND DEVICES

Elena Semouchkina,[1] Wenwu Cao,[1] and Raj Mittra[2]
[1] Materials Research Laboratory
The Pennsylvania State University
University Park, Pennsylvania 16802
[2] Department of Electrical Engineering
The Pennsylvania State University
University Park, Pennsylvania 16802

Received 18 September 1998

ABSTRACT: *Two different types of source excitation for finite-difference time-domain (FDTD) simulations, i.e., electric and magnetic field types, are investigated in this work for configurations that have no ground planes. This paper shows that the electric field excitation introduces errors in the computed admittance of the device due to the frequency dependence of the gap admittance, while the magnetic field excitation does not suffer from this drawback; consequently, the latter is better suited for circuit simulations.* © 1999 John Wiley & Sons, Inc. Microwave Opt Technol Lett 21: 93–100, 1999.

Key words: *finite-difference time domain; microwave devices; source excitation*

1. INTRODUCTION

The finite-difference time-domain method (FDTD) has been used extensively to model a wide variety of microwave problems [1–5]. Although introduced originally for the full-wave modeling of scattering phenomena [1], it was later extended to problems involving microstrip configurations [2–5]. Typically, a lumped circuit approach [5] is used in the FDTD method to evaluate the effects produced by microelectronic devices in microwave circuits. In such an approach, the physical device is replaced by its equivalent circuit, and this lumped circuit is then used as a termination for metallic transmission lines [5]. However, with an increase in the operation frequency of a device, its performance becomes strongly dependent on the geometry and material properties. One consequence of this is that, to determine the optimum electrical characteristics, as well as to assess the effect of the geometry of the microelectronic device, it becomes necessary to incorporate its real dimensions and parameters into the model. Another important aspect of the high-frequency simulation is the incorporation of a suitable source excitation, which is the focus of attention in this paper.

Usually, for microstrip problems, the excitation source may be either a distributed [2, 3] or a lumped source [5], and is located between the microstrip and the ground plane. For certain devices, however, the ground planes are either nonexistent, or the transmission line structure is excluded from the simulation to reduce the size of the FDTD computational domain. The introduction of a gap voltage source in the microstrip line without ground planes has been described in [6], although the problem of impedance computation using this type of source excitation was not discussed in that work. Two other contributions [7, 8] have pointed out that errors are introduced in the impedance results because such a source has a complex impedance of its own.

In this paper, two excitation methods are investigated in the context of the FDTD modeling of 3-D devices. The first of these utilizes a gap excitation of the electric field, which is analogous to a voltage source introduced in the microstrip gap, as described in [6]. The second approach employs a magnetic field excitation around the conductor, which has not apparently been reported in the published literature on FDTD simulations. We present the simulation results obtained by using these excitation methods, and compare them in both the time and frequency domains. Our study shows that the magnetic field excitation method appears to be more accurate for admittance calculations than the electric field method, which introduces errors due to the interference to the computed admittance from the complex gap admittance.

2. SOURCE EXCITATION

We focus on the problem of source excitations in FDTD simulations that launch an electric current in a conducting wire. This current, in turn, serves as an input source for an arbitrary circuit or device in the absence of any ground planes.

The method of electric field excitation in a wire gap is illustrated in Figure 1. In this scheme, the applied electric field has only an E_y-component directed along the wire. In [6], it was conjectured that the impedance of such a source is equal to the characteristic impedance of the microwave circuit to be modeled. However, our simulation results show that this assumption does not hold, even for a simple capacitor configuration.

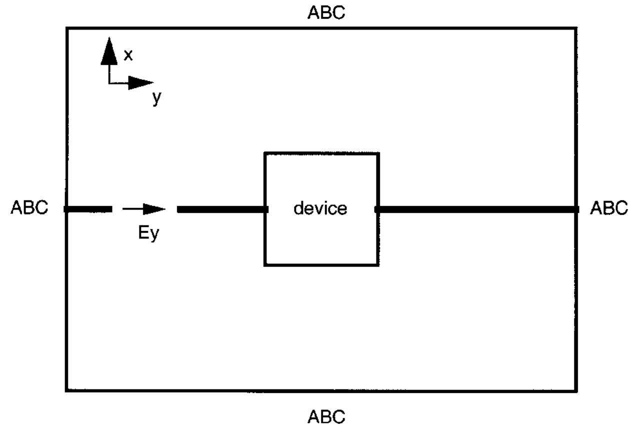

Figure 1 Electric field excitation in the gap of a conducting wire

Figure 2 illustrates the method of magnetic field excitation around the conducting wire. Two of the simplest ways for introducing this type of excitation are: 1) excite only two H_z (or H_x) magnetic field components that are equal in magnitude, but opposite in sign in the two FDTD cells closest to the wire from the opposite sides; and 2) excite both the H_x- and H_z-components in four cells around the wire, as illustrated in the inset in Figure 2, which shows the cross section along the wire direction. These two schemes differ only in the magnitudes of the electric current, with the current in method 2) being twice as large as that in method 1). The magnetic field excitation scheme does not require the presence of a gap in the conductor, and hence, contributes no errors in the simulated impedance of the circuit.

To compute the frequency dependence of the simulated parameters, a Gaussian-shaped pulse is used for both electric field and magnetic field excitations. The fast Fourier transform (FFT) procedure is then applied to convert the results of the time-domain simulation into the frequency domain. Also, absorbing boundary conditions [9] are placed along the FDTD mesh boundaries to suppress undesirable reflected waves. Finally, as demonstrated in the following section, both the electric and magnetic field excitation methods launch an electric current in the conducting wire, which serves as an input current for the circuit or device to be simulated.

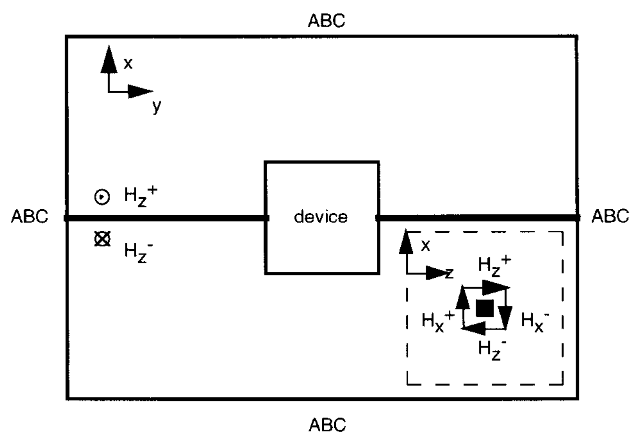

Figure 2 Magnetic field excitation around the conducting wire

Before closing this section, we mention that the analogs of the two excitation methods in wire antenna simulations are the delta-gap and magnetic frill sources [7], respectively.

3. NUMERICAL RESULTS

3.1. Conducting Wire. The electric field and magnetic field excitation schemes were first verified by using the example of a conducting wire, which is directed along the y-axis and has a square cross section of 1×1 cell. The cell sizes in the x-, y-, and z-directions all equal 5×10^{-5} m, and the time step for the simulation is chosen in accordance with the Courant condition, which is 9.53287×10^{-14} s. Either a symmetric FDTD mesh of $64 \times 64 \times 64$ cells or asymmetric ones with dimensions of $140 \times 170 \times 64$ and $140 \times 80 \times 35$ cells, respectively, are used for the simulation.

Figure 3 shows the current pulse propagating along a perfect electric conducting wire, modeled here by letting the conductance $\sigma = 10^{10}$ S/m. The bandwidth of the Gaussian-shaped electric field pulse is $f_b = 30$ GHz, and it excites a gap in the wire with a width of one cell, located at the sixth cell from the left. Figure 4 illustrates the rapid decay of the electric current pulse in the wire when its conductance is reduced to $\sigma = 10^3$ S/m. Figure 5 plots the current pulse propagating along the perfectly conducting wire for the case of two-sided magnetic field excitation (see Fig. 2), also at the sixth cell with $f_b = 30$ GHz.

Figures 6 and 7 depict snapshots of the magnetic and electric field distributions around the conductor, respectively, for a time step that corresponds to the maximum of the electric current. We note the similarity of the two plots, except in the source region (< 3 cells from the source). The above example shows that the two excitations appear to work equally well for this simple canonical geometry.

3.2. Capacitor. We turn to the case of a capacitor, which is inserted along the wire. The high-frequency performance of a capacitor is known to be strongly related to its geometry and material properties [10, 11], and considerable insight can be gained by simulating the performance of the selected design. The comparison study was carried out for a simple one-layer capacitor with plate dimensions of 30×30 cells and an electrode separation of three cells. The capacitor was air filled.

Figure 8 shows the time dependence of the voltage across the capacitor for both types of excitations, which utilize a Gaussian-shaped pulse with a bandwidth of 10 GHz. For the electric field gap source, only the charging process of the capacitor is observed because the presence of the gap prevents the capacitor from discharging. However, both charging and discharging of the capacitor occurs when the excitation is magnetic.

The electric field distribution in the computational domain is shown in Figure 9, and is similar for both types of source excitation. This distribution is a snapshot of the time step for which the voltage signal is a maximum. The fringing of the fields near the electrode edges, typical for the capacitor, is evident from this plot.

To determine the frequency dependence of the admittance of the capacitor, the voltage and current in the capaci-

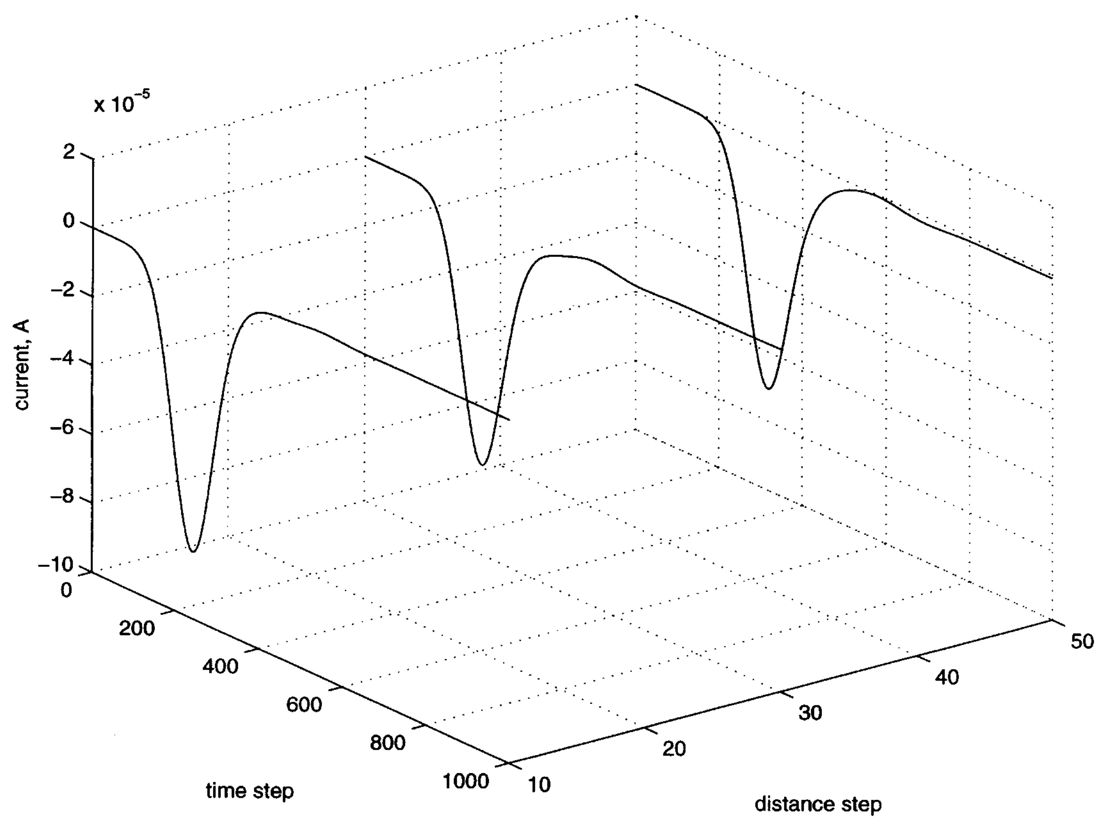

Figure 3 Electric current pulse propagating along the wire with a conductance of $\sigma = 10^{10}$ S/m following the excitation of an electric field Gaussian pulse ($f_b = 30$ GHz) in the gap

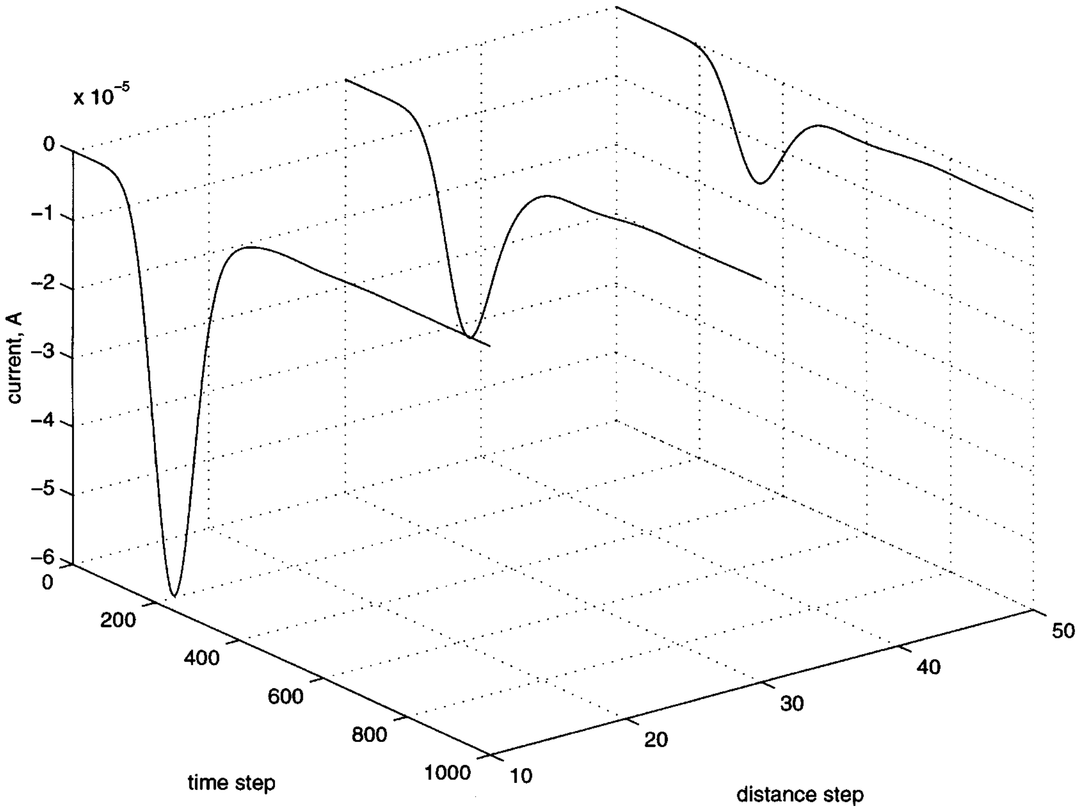

Figure 4 Electric current pulse propagating along the wire with a conductance of $\sigma = 10^3$ S/m following the excitation of an electric field Gaussian pulse ($f_b = 30$ GHz) in the gap

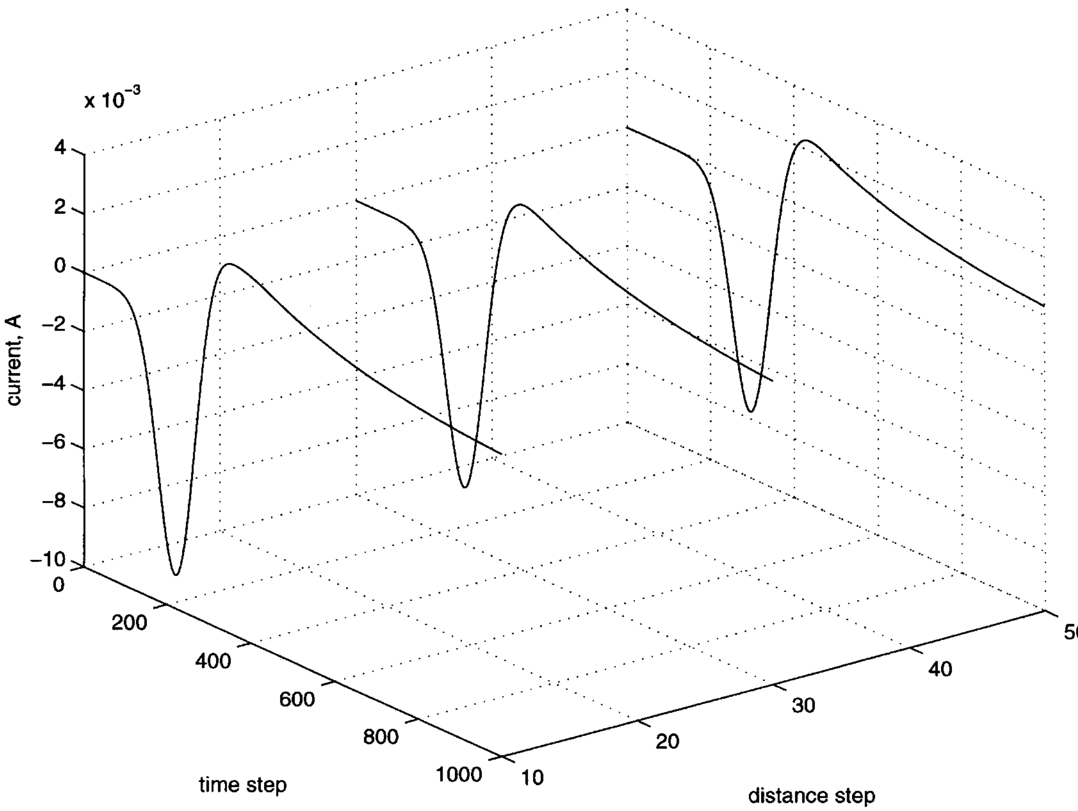

Figure 5 Electric current pulse propagating along the wire with a conductance of $\sigma = 10^{10}$ S/m following the excitation of magnetic field Gaussian pulse ($f_b = 30$ GHz) around the wire

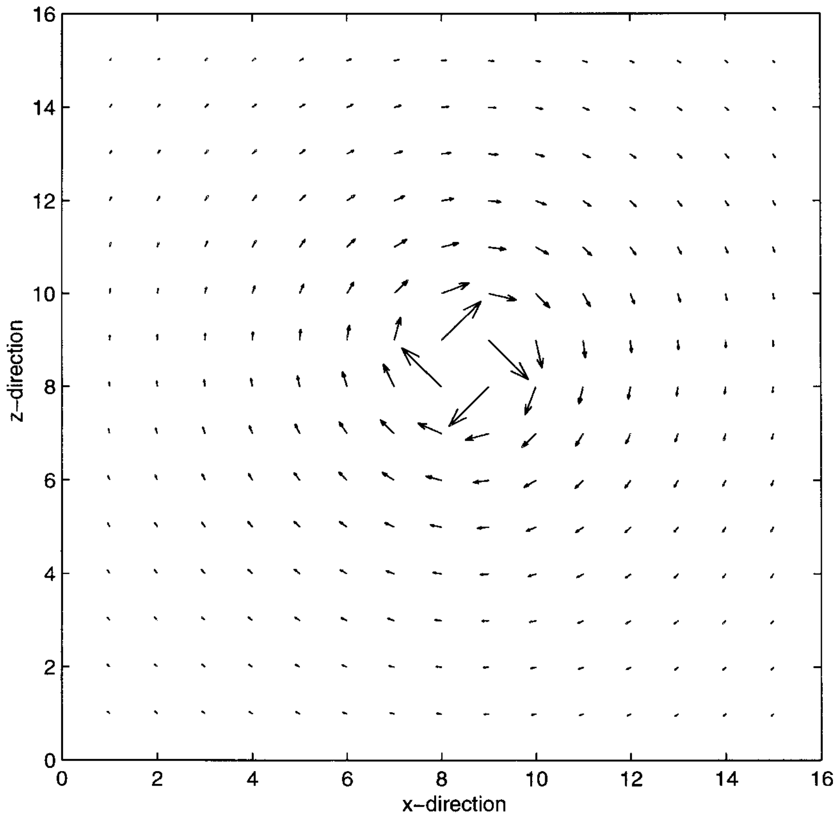

Figure 6 Magnetic field distribution around the conducting wire carrying an electric current

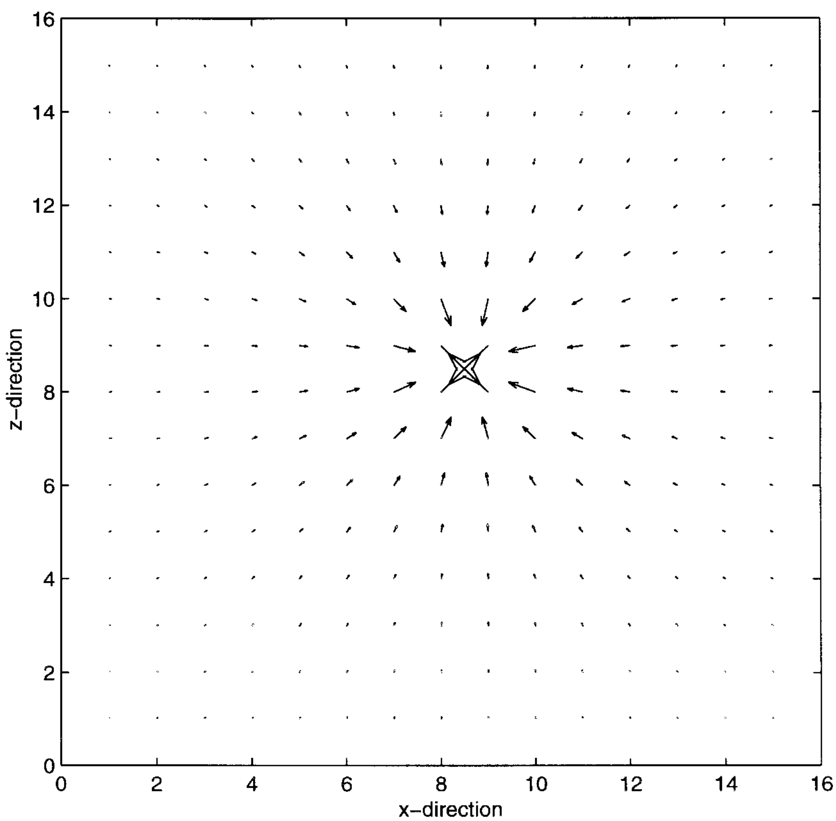

Figure 7 Electric field distribution around the conducting wire carrying an electric current

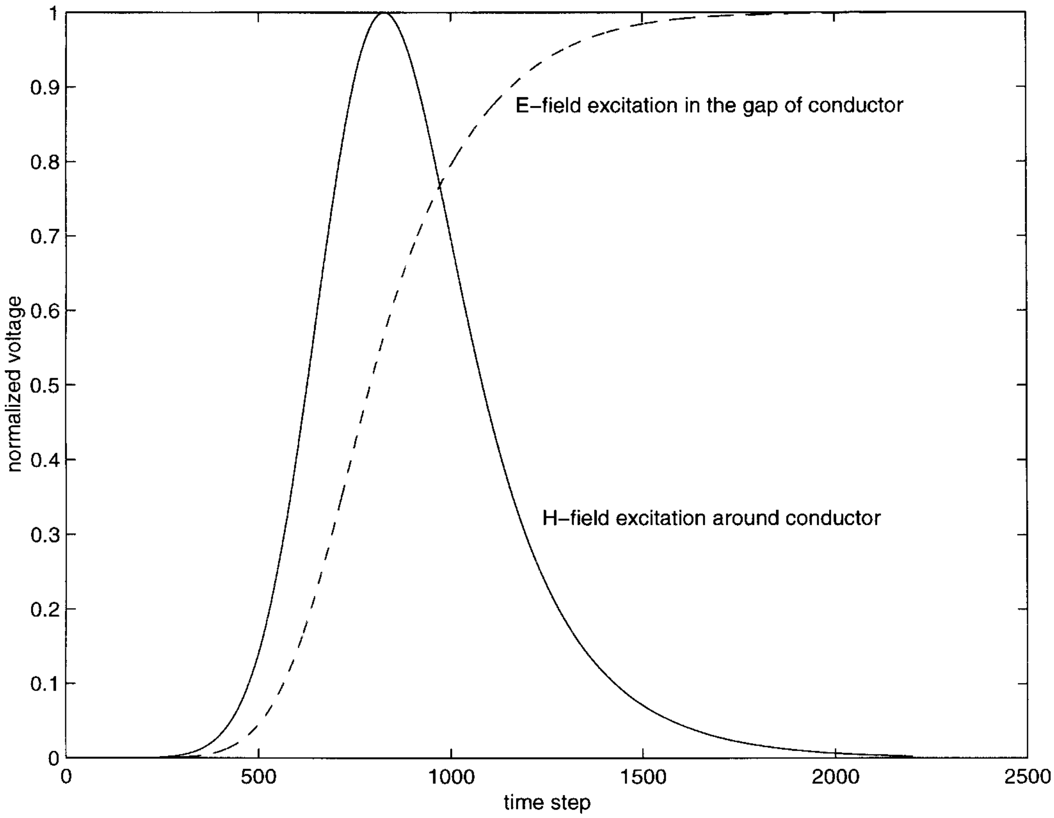

Figure 8 Voltage on the capacitor versus time using an electric field excitation in the gap as input (dashed curve) and a magnetic field excitation around the conductor to generate input (solid curve)

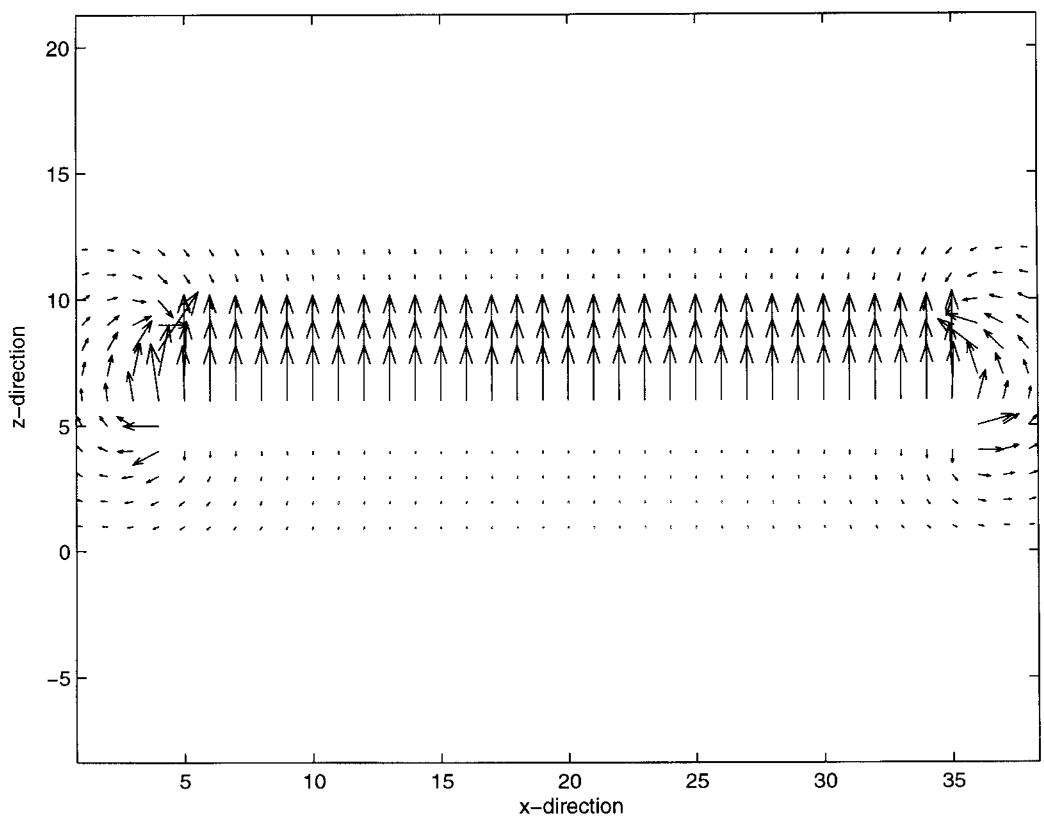

Figure 9 Electric field distribution inside and outside the capacitor for both excitation methods

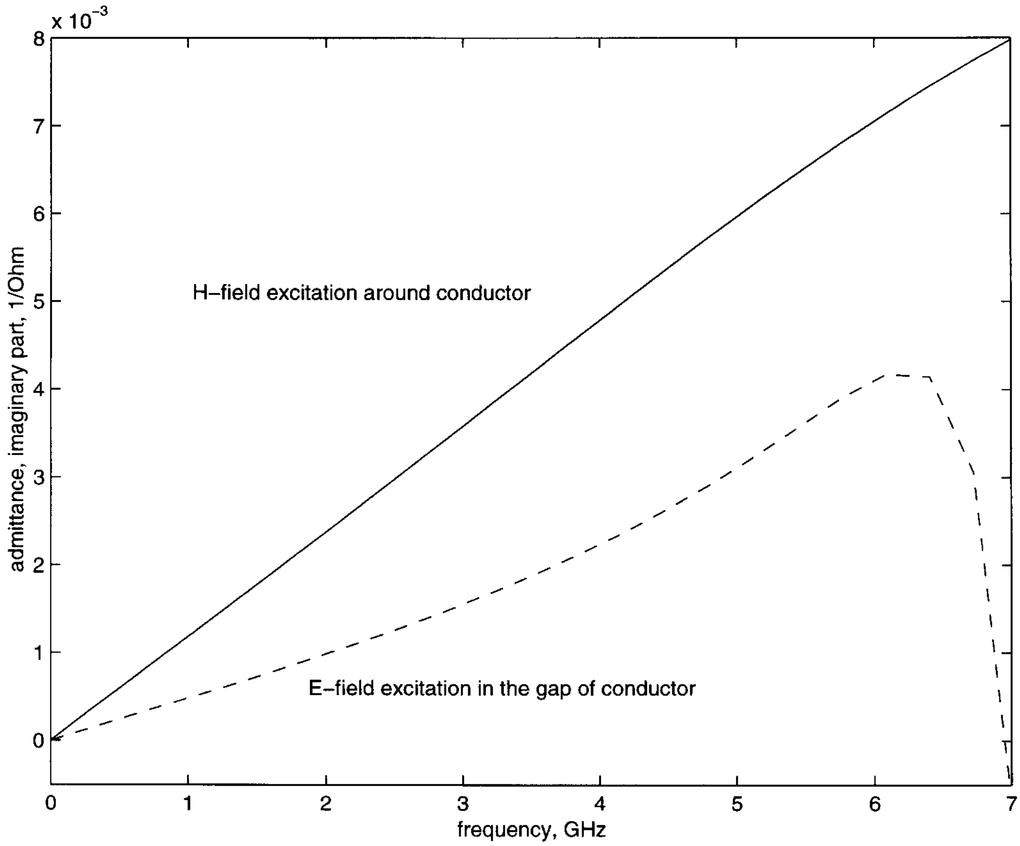

Figure 10 Frequency dependence of the imaginary part of the capacitor admittance computed by using the magnetic field (solid curve) and the electric field (dashed curve) excitations, respectively

tor are calculated from the time-domain data by using the FFT. For low frequencies, the capacitor admittance Y is expected to be a linear function of the frequency f, i.e., $Y = j\omega C$, where $\omega = 2\pi f$ and C is the capacitance. Figure 10 plots the imaginary part of the admittance versus frequency, derived by using both types of source excitation. The expected linear dependence is observed for the case of the magnetic field excitation, and the value of the capacitance, derived from the slope of this plot, was found to be 0.2 pF. This value is different from the 0.14 pF of the parallel plate approximation, which neglects the fringing fields [12]. Figure 10 shows that the linear dependence of the admittance imaginary part versus frequency is observed only in a narrow frequency range for the case of electric field excitation. The slope of this plot in the linear range corresponds to a capacitance value of 0.075 pF, and the difference of this value from the parallel plate capacitance of 0.14 pF cannot be explained by the fringing of fields [12]. Hence, this leads us to conclude that the computed capacitance value is in error. The source of this error is that the admittance of the gap source [7, 8] is frequency dependent, which is similar to the case of a resistive voltage source described in [8].

4. CONCLUSIONS

Two methods of source excitation for FDTD simulations of circuits, viz. the electric and magnetic field excitations, have been investigated in this paper, neither of which requires ground planes. While both of these excitation schemes generate electromagnetic field distributions that are very similar to each other, only the magnetic field excitation generates realistic results for the admittance. For the electric field excitation, the gap admittance causes the computed input admittance to deviate from the true value.

REFERENCES

1. K.S. Yee, Numerical solution of initial boundary value problems involving Maxwell's equations in isotropic media, IEEE Trans Antennas Propagat AP-14 (1966), 302–307.
2. X. Zhang, J. Fang, K.K. Mei, and Y. Liu, calculations of the dispersive characteristics of microstrips by the time-domain finite difference method, IEEE Trans Microwave Theory Tech 36 (1988), 263–267.
3. X. Zhang and K.K. Mey, Time-domain finite difference approach to the calculation of the frequency dependent characteristics of microstrip discontinuities, IEEE Trans Microwave Theory Tech 36 (1988), 1775–1787.
4. K.S. Kunz and R.J. Luebbers, Finite difference time domain method for electromagnetics, CRC Press, Boca Raton, FL, 1993.
5. M. Piket-May, A. Taflove, and J. Baron, FD-TD modeling of digital signal propagation in 3-D circuits with passive and active loads, IEEE Trans Microwave Theory Tech 42 (1994), 1514–1523.
6. X. Wang and R.J. Hwu, A new source formulation for FDTD simulation of high-frequency integrated circuits with and without ground plates, Microwave Opt Technol Lett 14 (1997), 321–324.
7. C.A. Balanis, Advanced engineering electromagnetics, Wiley, New York, 1989.
8. O.P.M. Pekonen, J. Xu, and K.I. Nikoskinen, Rigorous analysis of circuit parameter extraction from an FDTD simulation excited

with a resistive voltage source, Microwave Opt Technol Lett 12 (1996), 205–210.
9. G. Mur, Absorbing boundary conditions for the finite-difference approximation of the time-domain electromagnetic-field equations, IEEE Trans Electromag Compat EMC-23 (1981), 377–382.
10. A.T. Murphy and F.J. Young, High frequency performance of multilayer capacitors, IEEE Trans Microwave Theory Tech 43 (1995), 2007–2015.
11. L.W. Schaper and G. Morcan, High frequency characteristics of MCM decoupling capacitors, IEEE 46th ECTC Proc Orlando, FL, May 1996, pp. 358–364.
12. B. Beker, G. Cokkinides, and A. Templeton, Analysis of microwave capacitors and IC packages, IEEE Trans Microwave Theory Tech 42 (1994), 1759–1764.

CCC 0895-2477/99

MINIMIZATION OF CROSSTALK IN A FAST WDM SYSTEM USING AN ADAPTIVE ARRAY*

Chulhun Seo[1] **and Taesun Kim**[1]
[1] Department of Information and Telecommunication Engineering
Soongsil University
Seoul 156-743, Korea

Received 26 September 1998

ABSTRACT: *In this paper, an adaptive array algorithm is presented to minimize linear crosstalk in high-speed WDM systems. The algorithm is based on the optimum and the decision-directed algorithm added to the test signal sequences and sampling process. In transmitting data, the speed of algorithm processing reaches that of transmittance by a sampling process.* © 1999 John Wiley & Sons, Inc. Microwave Opt Technol Lett 21: 100–102, 1999.

Key words: *adaptive array algorithm; linear crosstalk; WDM*

1. INTRODUCTION

Linear crosstalk [1] originates from the imperfect channel-selection device, and depends on many factors such as the interchannel spacing and the demultiplexing elements used to select the channel. To decrease the crosstalk which limits the channel density, most research has focused on the development of strict demultiplexer, filter design, and fabrication techniques [2, 3], but it is difficult to get sharp characteristics. Several authors proposed other methods such as the least mean-square (LMS) algorithm [4] to cancel the crosstalk in a WDM system. An optimal receiver filter was derived for a multichannel digital receiver by Salz [5]. Recently, Minardi and Ingram [6, 7] proposed two adaptive algorithms to reduce the linear crosstalk in dense WDM systems. Their algorithms do not require training sequences for initialization. These algorithms make transmission with dense channels possible, and improve the channel capacity by minimizing the crosstalk. But it is very difficult to have high-speed signal processing corresponding to optical communication. The performance also degrades in the initial stage when applying these algorithms because the initial values take arbitrary values and search for the optimum weights. In this paper, the algorithm has been used with test signal sequences and the sampling process to speed up the process. The header of the transmitted signal is used to initiate initial weights of the decision-directed adaptive array algorithm. It is employed in transmitting data by using the optimum adaptive array algorithm. We propose that the algorithms are applied to a subsequence of the data stream to speed up the transmittance of the data signal. Namely, one of every large number of bits is used for adapting the WDM system. The sampling operation is possible because the integrated module of the WDM receiver including the demultiplexer is stable. Therefore, this adaptive array algorithm will be a very good alternative, requiring perfect performance of the demultiplexer and filter in WDM systems.

* This work is supported by the Ministry of Information and Communication and Soonsil University.

2. MINIMIZATION OF CROSSTALK

Figure 1 shows a block diagram of the WDM receiver with the adaptive array algorithm, the sampling process, and the crosstalk level monitoring. WDM channels are demultiplexed by a grating, photodetected by the detector array and weighted by the weight vector which is found from the adaptive array algorithm. These signals are summed and digitized by the threshold device. The detector output is a linear combination of the detected signal from all channels (n-channels) plus the detector thermal noise resulting from imperfections in the demultiplexer. The detector array (m-detectors) outputs can be represented by the matrix $\mathbf{Z}$, such that $\mathbf{Z} = \mathbf{GS} + \mathbf{v}$, where $\mathbf{Z}$ is an $m \times 1$ matrix and the ith row of $\mathbf{Z}$ describes the output of the ith detector. $\mathbf{S}$ and $\mathbf{v}$ are vectors of n-channel signals without crosstalk and m-detector thermal noise, and $\mathbf{G}$ is a matrix of crosstalk gains of detectors where g_{ij} is the detect gain of the jth channel signal by the ith detector. $\mathbf{G}$ can be divided into the light distribution of the desired channel signal to the detector array $\mathbf{G}_d$ and the element of undesired channel signals $\mathbf{G}_c$. $\mathbf{S}$ can also be split into the desired channel signals S_d and the undesired channel signals $\mathbf{S}_c$. So the detector array outputs can be described as $\mathbf{Z} = \mathbf{G}_d S_d + \mathbf{G}_c \mathbf{S}_c + \mathbf{v}$, which consists of the desired signal, crosstalk (undesired) signal, and detector noise components. The detector outputs are weighted and summed to minimize crosstalk in the high-speed WDM system. It produces the overall system output $\mathbf{S}_{\text{out}} = \mathbf{W}^T\mathbf{Z}$ and is digitized by the threshold device. An adaptive array algorithm is employed to find the optimum weights $\mathbf{W}$ which maximize the ratio of desired signal energy to (crosstalk plus noise) signal energy (SCNR) in the high-speed WDM system. The overall SCNR is given by [7]

$$\text{SCNR} = \frac{\langle S_d^2 \rangle \mathbf{W^T G_d G_d^T W}}{\mathbf{W^T (G_c \langle S_c S_c \rangle G_c^T} + \sigma^2 \mathbf{I)W}} \qquad (1)$$

where σ^2 is the noise power. The algorithms run independently in each channel, and the number of algorithm units should be equal to the number of channels. Optimum weights are commonly found from the mean-square error (MSE) defined as the variance of the difference between the weighted output and the desired signal. The MSE can be expressed by $\mathbf{W^T Z} - S_d$. The optimum weights which minimize MSE are described by the Wiener–Hopf equation as follows [4]:

$$\mathbf{W}_{\text{MSE}} = (\mathbf{G} \langle \mathbf{S}_d \mathbf{S}_d^T \rangle \mathbf{G}^T + \sigma^2 \mathbf{I})^{-1} \mathbf{G} \langle \mathbf{S} S_d \rangle. \qquad (2)$$

The standard LMS algorithm which uses the negative gradient of the squared error $-\Delta_{\mathbf{W}}(\langle e^2 \rangle)$ as a noisy estimate can